Chapter 4

Single Phase Wireless Electric Vehicle Charger Using EF_2 Inverter

4.1 Introduction

Wireless charging of electric vehicle (EV) offers a convenient and hassle free charging experience to the EV users that do not use any kind of physical contact between the power supply and the vehicle. The user just need to park at the designated place and the transmitting unit is fitted there beneath the ground level. A pictorial representation of a typical single-phase domestic/commercial wireless EV charging system is represented in Fig. 4.1. It can be observed from Fig. 4.1 that the powertrain architecture for the wireless charging of EV contains three major sections, which are: transmitting unit, WPT system and receiving unit. The most important part in the wireless power transfer (WPT) system is to generate sinusoidal AC wave (voltage/current) at very high frequency as discussed in the literature survey of chapter 1. The various high frequency inverter (HF inverter) topologies related to wireless EV charging are studied, which are generally used as a part of the transmitting unit that generate sinusoidal waveforms at very high frequency. The major lacunas of the conventional wireless EV chargers are listed below.

1) Require a high voltage DC source,
2) Use topology with multiple switches
3) Hard switching of the MOSFETs in the HF inverter,
4) Do not support varying conditions and
5) Do not support both CC and CV charging operation.

In order to solve the above issues, a novel wireless battery charger topology for EV applications is proposed in this chapter that can be installed in public charging infrastructure and in home premises. The proposed topology can maintain constant current (CC) as well as constant voltage (CV) at the battery terminal, and simultaneously can maintain near unity power factor (UPF) at the input side using power factor correction (PFC) operation, and thus satisfies all the criteria of a standard EV charger.

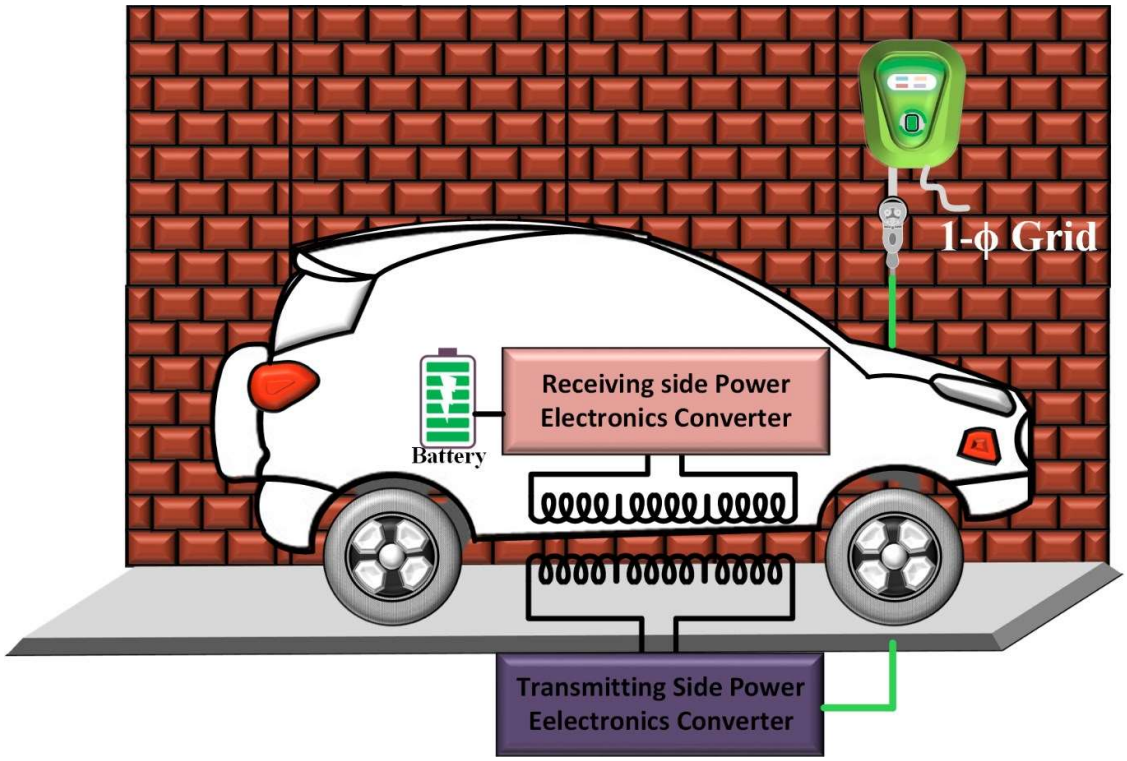

Fig. 4.1. A pictorial representation of a typical wireless EV charging facility.

The heart of the wireless power transfer (WPT) scheme is a HF inverter. In this work, a class EF_2 inverter is used to generate high frequency AC (HFAC) in such a way that it can deliver power with variable loading condition, while maintaining a constant current or a constant voltage according to the requirement of CC-CV charging profile. To supply power to the EF_2 inverter, an AC-DC front-end converter (stage-I) is integrated with the charger. The stage-I is operated as a constant voltage source to the EF_2 inverter for CC mode and constant current source for CV mode operation. The CC-CV at the battery end and PFC at the input end are achieved only by controlling the gate pulse of stage-I. The WPT coils are first simulated using Ansys Maxwell package and the complete charger is simulated using PSIM simulation software. A scaled-down laboratory prototype of the proposed charger is developed and tested with resistive load to validate the idea. The wireless power transfer is achieved for a maximum distance of 12 cm between the transmitting and receiving coil. Finally, the proposed charger is tested to charge a 24 V battery pack and the CC-CV charging profile for the same is presented in this chapter.

4.2 Proposed Wireless EV Charger

The proposed charger taps power from the single-phase utility supply and wirelessly charges the battery set of EV. The circuit diagram of the proposed topology is shown in Fig. 4.2. The proposed circuit is divided into four major sub-sections: i) AC-DC boost converter, ii) DC-HFAC resonant inverter, iii) wireless power transfer scheme and iv) rectifier unit.

As discussed earlier, a HF inverter is the heart of WPT scheme. A load independent EF_2 inverter is used to produce high frequency sinusoidal AC. The HF inverter produces constant AC current, when excited with constant DC voltage and produces constant AC voltage, when the input of the inverter is a constant DC current source. To accommodate either a constant DC voltage source or a constant DC current source at the input of the inverter, an AC-DC front-end converter is selected as stage-I. The front-end converter is responsible to deliver power to the EF_2 inverter at constant voltage or constant current, while maintaining the input power factor to near unity. The WPT scheme uses magnetic resonance coupling (MRC) technique to transfer power from the transmitting side to the receiving side wirelessly. This consists of two coils (viz. primary and secondary) with their corresponding matching networks. The primary coil draws power from the inverter and transmits it to the secondary coil. The HFAC received at the secondary coil is converted to DC by a full-bridge diode rectifier that charges the battery.

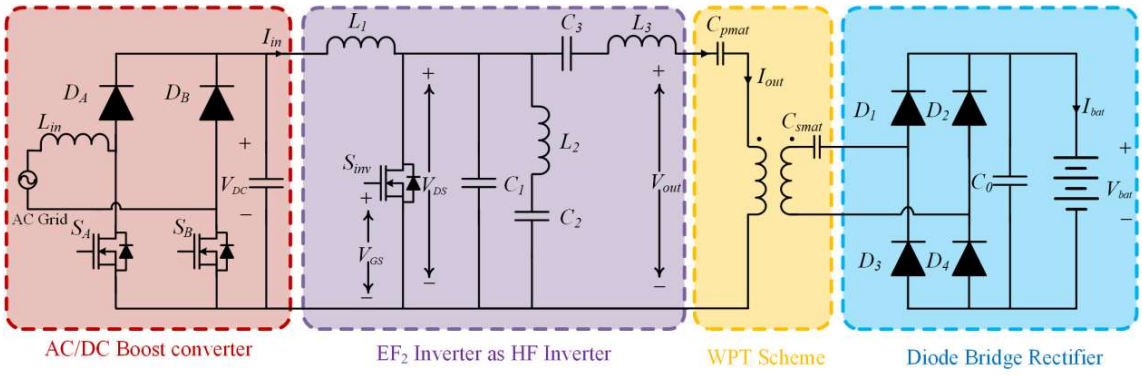

Fig. 4.2. Complete circuit schematics of the proposed Wireless EV charger.

4.3 Operation and Design of Proposed Wireless EV Charger

4.3.1 Stage I: AC-DC Boost Converter

A bridge-less PFC structure with two switches on the lower side, two diodes on the upper side and an inductor at the input is used as an AC-DC boost convertor. This stage is responsible to deliver DC power to the HF inverter, and to maintain near unity power factor at the grid side. The main objective of this stage is to deliver power to the HF inverter at constant DC voltage or constant DC current as required by the CC-CV charging logic. The inductor at the input side acts as a boost inductor for this stage. The operation of this stage is described with four modes of operations in chapters 2 and 3.

4.3.2 Stage II: High Frequency EF_2 Inverter

The proposed schematic uses an EF_2 inverter to produce HFAC voltage or current according to the requirement of CC-CV charging algorithm. This inverter is also capable to deliver power at constant current or constant voltage to a load with variable resistance. The Fig. 4.3 shows the circuit representation of class EF_2 inverter that supports both CC and CV modes of operation by delivering constant AC current or constant AC voltage during CC mode and CV mode, respectively. Mathematical analysis and design of the EF_2 inverter for load independent condition is elaborated in section 4.4.

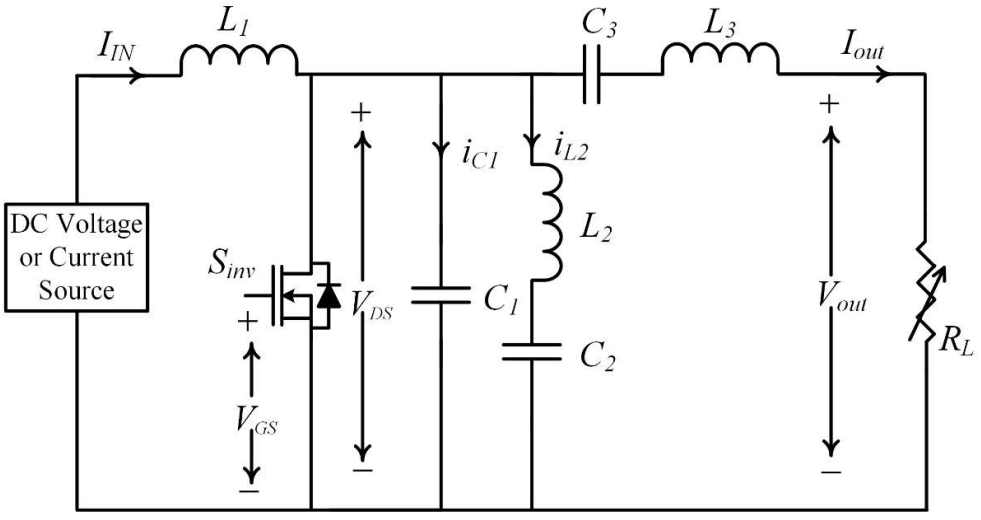

Fig. 4.3. Circuit diagram of EF_2 inverter.

4.3.3 Stage III: Wireless Power Transfer Scheme

The transmitting and receiving coils are designed according to the required current rating. Series-series topology is considered as the compensating network for MRC. A combination of capacitor in series with the coil at both transmitting and receiving side forms the WPT section as shown in Fig. 4.2. The values of these capacitors (C_{pmat} and C_{smat}) are designed to resonate with the corresponding coil inductances at the operating frequency using $f_s = \frac{1}{2\pi\sqrt{LC}}$. Same number of turns are used in both transmitting and receiving side coils, which facilitate to use same values of capacitances in both sides, i.e., $C_{pmat} = C_{smat}$.

4.3.4 Stage IV: Rectifier Unit

The rectifier unit uses a full-bridge diode rectifier to convert the HFAC to DC as shown in Fig. 4.2. The selection of diodes is one of the major concerns, as the high frequency operation requires less reverse recovery time. The output capacitor of this unit is designed to minimize the ripple in the output voltage.

4.4 Mathematical Analysis of EF_2 Inverter

The detailed operation and its corresponding mathematical analysis are provided in this section. The equivalent circuit diagrams of the EF_2 inverter during ON state and OFF state of the switch S_{inv} are presented in Fig. 4.4 and Fig. 4.5, respectively.

4.4.1 During $0 \leq \omega t \leq 2\pi D$ (Sinv is ON)

When the inverter is excited with a constant DC voltage source, assuming a sinusoidal output current of the inverter,

$$I_o(\omega t) = I_m \sin(\omega t + \phi) \tag{4.1}$$

where I_m denotes the peak of the output current and ϕ is its phase angle.

The switch S_{inv} is kept ON for time $\omega t \in [0, 2\pi D]$, where D denotes the duty cycle of the switch. The equivalent circuit during this period is presented in Fig. 4.4.

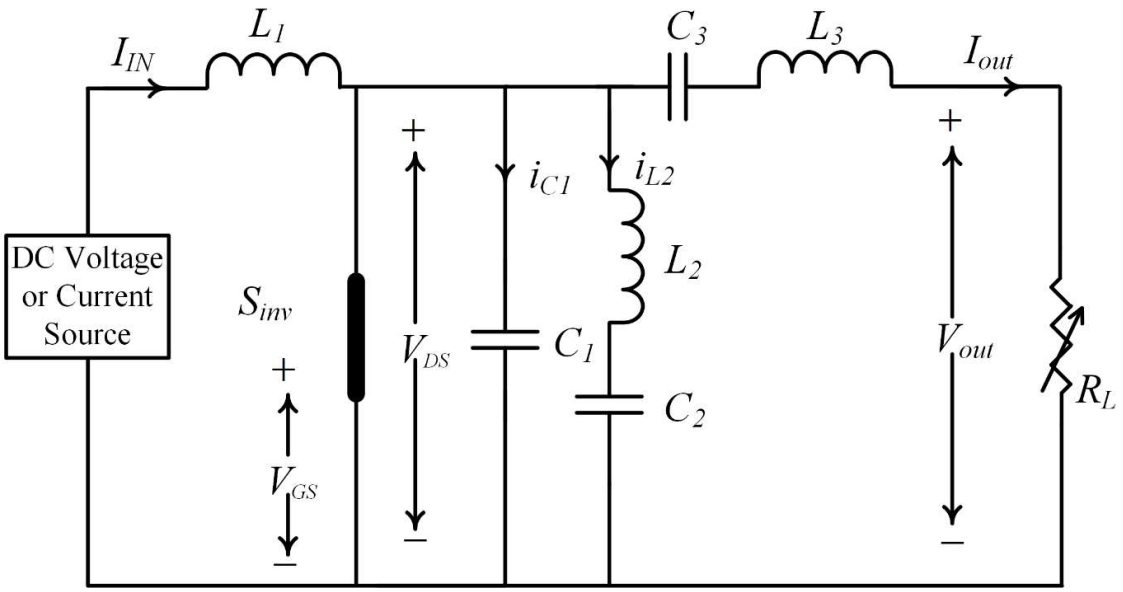

Fig. 4.4. Equivalent circuit diagram of inverter during ON period.

During this period, as the switch is short circuited, the voltage across the switch S_{inv}

$$v_{DS}(\omega t) = 0 \tag{4.2}$$

and the current through the capacitor C_1 is

$$i_{C_1}(\omega t) = 0 \tag{4.3}$$

Also, for $0 \leq \omega t \leq 2\pi D$ the voltage $v_{DS}(\omega t)$ can be written as

$$v_{DS}(\omega t) = \omega L_2 \frac{di_{L_2}}{d\omega t} + \frac{1}{\omega C_2}\int i_{L_2}(\omega t) d\omega t = 0 \tag{4.4}$$

Differentiating (4.4) and multiplying it by $\frac{1}{I_{IN}}$

$$\frac{1}{I_{IN}}\left(\omega L_2 \frac{d^2 i_{L_2}}{d\omega t^2} + \frac{i_{L_2}(\omega t)}{\omega C_2}\right) = 0 \tag{(4.5}$$

Substituting $\frac{i_{L_2}(\omega t)}{I_{IN}} = e^{r\omega t}$ in (4.5), and solving the quadratic equation, roots r can be written as

$$r = \pm\frac{j}{\omega\sqrt{L_2 C_2}} = \pm q_1 \tag{4.6}$$

The general solution for (4.4) can be written as

$$\frac{i_{L_2}(\omega t)}{I_{IN}} = Ae^{+jq_1\omega t} + Be^{-jq_1\omega t} \tag{4.7}$$

$$= A(\cos(q_1\omega t) + j\sin(q_1\omega t)) + B(\cos(q_1\omega t) - j\sin(q_1\omega t))$$
$$= A_1\cos(q_1\omega t) + B_1\sin(q_1\omega t)$$

where A and B are the constants, $A_1 = A + B$ and $B_1 = (A - B)j$.

The constants A_1 and B_1 are arbitrary constants considered for solving the differential equations and the corresponding values are to be determined based on the boundary conditions, which means continuous voltage and current waveforms are obtained at the switching instants (when switch is turned ON or turned OFF).

By applying Kirchhoff's current law at the switch node in Fig. 4.4, the current $i_s(\omega t)$ through the switch S_{inv} can be written as

$$i_s(\omega t) = I_{IN} - i_{L_2}(\omega t) - i_o(\omega t) - i_{C_1}(\omega t) \tag{4.8}$$

$$i_s(\omega t) = I_{IN} - A_1\cos(q_1\omega t) - B_1\sin(q_1\omega t) - i_m\sin(\omega t + \varphi) \tag{4.9}$$

$$(\ as\ i_{C_1}(\omega t) = 0\ \text{ for } 0 \le \omega t \le 2\pi D\ )$$

4.4.2 During $2\pi D \le \omega t \le 2\pi$ (Sinv is OFF)

The switch S_{inv} is turned OFF for time $\omega t \in [2\pi D, 2\pi]$. The current through the switch is zero as the switch is OFF during this period. This gives

$$i_S(\omega t) = 0\ for\ 2\pi D \le \omega t \le 2\pi \tag{4.10}$$

Applying Kirchhoff's current law at the switch node, the current $i_{L_2}(\omega t)$ through inductor L_2 is given as

$$i_{L_2}(\omega t) = I_{IN} - i_{C_1}(\omega t) - i_o(\omega t) - i_s(\omega t) \tag{4.11}$$

$$= I_{IN} - i_{C_1}(\omega t) - i_m\sin(\omega t + \varphi) \quad (\text{as } i_o = i_m\sin(\omega t + \varphi))$$

$$= I_{IN} - \omega C_1\frac{dv_{DS}(\omega t)}{d\omega t} - i_m\sin(\omega t) \tag{4.12}$$

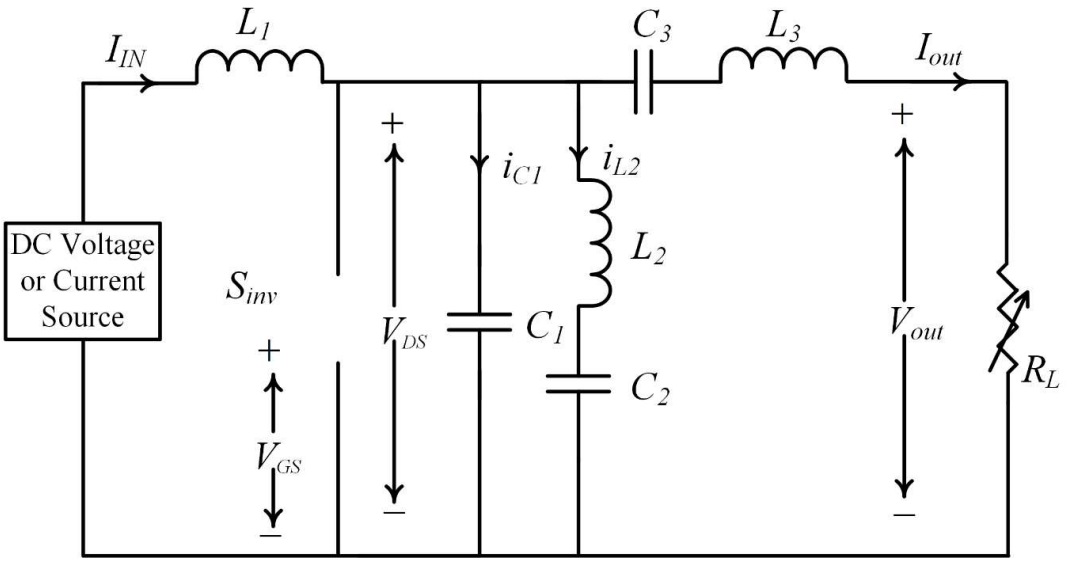

Fig. 4.5. Equivalent circuit diagram of inverter during OFF period.

The voltage across the switch S_{inv} during this mode $\omega t \in [2\pi D, 2\pi]$ can be represented by

$$v_{DS}(\omega t) = v_{L_2}(\omega t) + v_{C_2}(\omega t) = \omega L_2 \frac{di_{L_2}(\omega t)}{d\omega t} + v_{C_2}(\omega t) \tag{4.13}$$

where $v_{C_2}(\omega t)$ denotes the voltage across the capacitor C_2 and is given by

$$v_{C_2}(\omega t) = v_{C_2}(2\pi D) + \frac{1}{\omega C_2}\int_{2\pi D}^{\omega t} i_{L_2}(\tau)d\tau \tag{4.14}$$

Using (4.12), (4.13) and (4.14), and normalizing $i_{L_2}(\omega t)$ with respect to I_{IN}, the ratio $\frac{i_{L_2}(\omega t)}{I_{IN}}$ is given as

$$\frac{i_{L_2}(\omega t)}{I_{IN}} = 1 - \omega^2 L_2 C_1 \frac{d^2 \frac{i_{L_2}(\omega t)}{I_{IN}}}{d\omega t^2} - \frac{i_m}{I_{IN}} \sin(\omega t + \varphi) + \frac{C_1}{C_2}\frac{i_{L_2}(\omega t)}{I_{IN}} \tag{4.15}$$

It can be observed that (4.15) is a second order differential equation of $\frac{i_{L_2}(\omega t)}{I_{IN}}$. Solving the homogeneous and particular solution, the general solution can be written as the sum of homogeneous and particular solution and is given as

$$\frac{i_{L_2}}{I_{IN}}(\omega t) = A_2 \cos(q_2 \omega t) + B_2 \sin(q_2 \omega t) - \frac{\sin(\omega t + \phi) q_2^2 p}{q_2^2 - 1} + \frac{1}{k+1} \tag{4.16}$$

for $2\pi D \leq \omega t \leq 2\pi$

where $\frac{i_{L_2}}{I_{IN}}(\omega t) = A_2 \cos(q_2 \omega t) + B_2 \sin(q_2 \omega t)$ is the homogeneous solution and $\frac{i_{L_2}}{I_{IN}}(\omega t) = \frac{1}{k+1} - \frac{\sin(\omega t+\phi) q_2^2 p}{q_2^2 - 1}$ is the particular solution and the constants $k = \frac{C_1}{C_2}$, $q_2 = q_1\sqrt{\frac{k+1}{k}}$, $p = \frac{I_m}{I_{in}}\frac{1}{k+1}$. The constants A_2 and B_2 are determined from the boundary conditions for voltage and current continuity at the switching transitions.

The voltage $v_{DS}(\omega t)$ across S_{inv} can be written as

$$v_{DS}(\omega t) = \frac{I_{IN}}{\omega C_1}\int_{2\pi D}^{\omega t} \frac{i_{C_1}(\omega t) d\omega t}{I_{IN}} = \frac{I_{IN}}{\omega C_1}\gamma(\omega t) \tag{4.17}$$

The average voltage across the switch S_{inv} is equal to the input voltage V_{IN} and is given as

$$V_{IN} = \frac{I_{IN}}{2\pi\omega C_1}\int_{2\pi D}^{2\pi}\int_{2\pi D}^{\omega t} \frac{i_{C_1}(\tau) d\tau}{I_{IN}} d\omega t = \frac{I_{IN}}{2\pi\omega C_1}\int_{2\pi D}^{2\pi} \gamma(\omega t)\, d\omega t \frac{I_{IN}}{2\pi\omega C_1}\alpha \tag{4.18}$$

where

$$\alpha = \int_{2\pi D}^{2\pi} \gamma(\omega t)\, d\omega t \tag{4.19}$$

In summary, the current through different branches and voltage across different branches of the circuit can be written as follows:

1. The normalized **switch current** with respect to the input current $\frac{i_s}{I_{in}}(\omega t)$ can be written as

$$\frac{i_s}{I_{IN}}(\omega t) = \begin{cases} 1 - p(k+1)\sin(\omega t + \phi) - A_1 \cos(q_1 \omega t) - B_1 \sin(q_1 \omega t), & 0 \leq \omega t < 2\pi D \\ 0, & 2\pi D \leq \omega t < 2\pi \end{cases} \tag{4.20}$$

2. The **normalized current through the capacitor C_1** is given by

$$\frac{i_{C_1}}{I_{IN}}(\omega t) = \begin{cases} 0 & , \quad 0 \le \omega t < 2\pi D \\ 1 - p(k+1)\sin(\omega t + \varphi) - \dfrac{i_{L_2}(\omega t)}{I_{IN}}, & 2\pi D \le \omega t < 2\pi \end{cases} \tag{4.21}$$

where

$$\frac{i_{L_2}(\omega t)}{I_{IN}} = A_2\cos(q_2\omega t) - B_2\sin(q_2\omega t) + \frac{\sin(\omega t+\phi)q_2^2 p}{q_2^2-1} - \frac{1}{k+1} \tag{4.22}$$

3. The **normalized current through the Inductor L_2** is given by:

$$\frac{i_{L_2}}{I_{IN}}(\omega t) = \begin{cases} A_1\cos(q_1\omega t) + B_1\sin(q_1\omega t) & , 0 \le \omega t < 2\pi D \\ A_2\cos(q_2\omega t) - B_2\sin(q_2\omega t) + \dfrac{\sin(\omega t+\phi)q_2^2 p}{q_2^2-1} - \dfrac{1}{k+1} & , 2\pi D \le \omega t < 2\pi \end{cases} \tag{4.23}$$

4. The **normalized voltage across the Switch S_{inv}** is given

$$\frac{v_{DS}}{V_{IN}}(\omega t) = \begin{cases} 0 & , \quad 0 \le \omega t < 2\pi D \\ \dfrac{2\pi\gamma(\omega t)}{\alpha} & , \quad 2\pi D \le \omega t < 2\pi \end{cases} \tag{4.24}$$

4.4.3 ZVS and ZVDS and Boundary Conditions

The boundary conditions refer to the current and voltage continuity at the switching instants (the instants just before and just after the switch is either turned ON or OFF). These conditions can be written as

$$i_{L_2}(2\pi D^-) = i_{L_2}(2\pi D^+) \tag{4.25}$$

$$i_{L_2}(0) = i_{L_2}(2\pi) \tag{4.26}$$

$$\frac{di_{L_2}(\omega t)}{d\omega t}\Big|_{\omega t=2\pi D^-} = \frac{di_{L_2}(\omega t)}{d\omega t}\Big|_{\omega t=2\pi D^+} \tag{4.27}$$

$$\frac{di_{L_2}(\omega t)}{d\omega t}\Big|_{\omega t=0} = \frac{di_{L_2}(\omega t)}{d\omega t}\Big|_{\omega t=2\pi} \tag{4.28}$$

The boundary conditions for current continuity through the inductor L_2 for instants just before and after the switch is turned OFF and the instants just before and after the switch is turned ON are represented by (4.25) and (4.26). Similarly, (4.27) and (4.28) represent the boundary conditions for voltage continuity across the inductor L_2.

The zero voltage switching (ZVS) refers to the switching instance when the voltage across the switch is zero. The ZVS condition helps in decreasing the switching losses. It reduces the turn on losses and the voltage stress across the switch during turn on.

The zero voltage derivative switching (ZVDS) refers to the switching at the instant when the derivative of the voltage across the switch is zero. The ZVDS prevents the current stress of the switch as the capacitor discharges when the switch is turned on.

The fundamental component of the normalized switch voltage (with respect to the input voltage V_{in}) can be written using KVL as

$$\frac{v_{DS}}{V_{IN}}(\omega t) = \frac{i_m R_L}{V_{IN}}\sin(\omega t + \varphi) + \frac{i_m \omega L_x}{V_{IN}}\cos(\omega t + \varphi) \tag{4.29}$$

Using the Fourier analysis and (4.24), the coefficients $\frac{i_m R_L}{V_{IN}}$ and $\frac{i_m \omega L_x}{V_{IN}}$ can be written as

$$\frac{i_m R_L}{V_{IN}} = \frac{1}{\pi}\int_{2\pi D}^{2\pi} \frac{v_{DS}}{V_{IN}}(\omega t)\sin(\omega t + \varphi)d\omega t = \frac{2}{\alpha}\int_{2\pi D}^{2\pi} \gamma(\omega t)\sin(\omega t + \varphi)d\omega t = \frac{2}{\alpha}\psi_1(p) \tag{4.30}$$

$$\frac{i_m \omega L_x}{V_{IN}} = \frac{2}{\alpha}\int_{2\pi D}^{2\pi} \gamma(\omega t)\cos(\omega t + \varphi)d\omega t = \frac{2}{\alpha}\psi_2(p) \tag{4.31}$$

Since losses in the circuit is neglected, $P_{in} = P_{out}$. This gives

$$V_{IN} I_{IN} = \frac{1}{2} i_m^2 R_L \tag{4.32}$$

Using (4.30), (4.31) and (4.32)

$$\frac{\alpha(p)}{\psi_1(p)} = \frac{i_m}{I_{IN}} = p(k+1) \tag{4.33}$$

The loading parameter p is proportional to the magnitude of peak current, (4.33) can be rewritten as

$$p\frac{\psi_1(p)}{\alpha(p)} = \frac{1}{k+1} \tag{4.34}$$

For constant output AC current, the variation of (4.34) with respect to p should be zero for a range of p. Therefore

$$\frac{\partial}{\partial p}\left(p\frac{\psi_1(p)}{\alpha(p)}\right) = 0 \; over \; D_p \tag{4.35}$$

The four equations obtained from the boundary conditions, one obtained from the ZVS condition and (4.35) constitute a set of six equations with seven variables. After suitably selecting a value of p, $\psi_1(p)/\alpha(p)$ is calculated. Now the system has seven equations and seven variables, and thus can be solved for all seven unknowns.

$$I_m = 2\,\frac{\psi_1(p)}{\alpha(p)}\frac{V_{IN}}{R_L} \tag{4.36}$$

The maximum input current for the given values of I_m, R_L and $\psi_1(p)/\alpha(p)$ can be calculated using (4.36).

Using all the aforementioned conditions, and considering the maximum power output capability (q_l=1.66 and k= 1.2706) as discussed in [94], the expressions for the circuit parameters at 200 kHz are found as given in Table 4.1. The same expressions are also valid for constant voltage operation.

Table 4.1. Expressions for EF_2 circuit parameters

Parameter	Expressions
C_1	$\frac{1.41011}{R_L \times 10^7}$
C_2	$\frac{C_1}{1.2706}$
L_x	$\frac{2.1543}{C_1 \times 10^{13}}$
L_3	$\frac{7.95 \times Q * R_L}{10^7}$
C_3	$\frac{6.3325}{(L_3 - L_x) \times 10^{13}}$
L_2	$\frac{2.2980}{C_2 \times 10^{13}}$

4.5 Control Scheme for the Proposed Wireless EV Charger

The most important part of the proposed transmitting side topology is the EF_2 inverter. The closed-loop operation of such a HF inverter is difficult, as this require the sensing of HF inverter output parameters. The sensing of high frequency parameter require even higher frequency of controller operation. To avoid these issues, the EF_2 inverter is operated with constant duty ratio and constant switching frequency.

This HF inverter requires a regulated voltage or current source at its input for CC-CV operation. To achieve this, the front-end converter (stage-I) needs to be operated accordingly. For the front-end converter to supply regulated voltage/current at its output terminal, its output voltage and current need to be sensed. But, as the EF_2 inverter is operated at constant duty cycle, the required voltage and current at the battery terminals can be multiplied by a gain factor to find the new reference values of voltage or current at the output of stage-I. Therefore, instead of sensing voltage and current at the output of stage-I, these can be sensed at the battery terminals and corresponding gain factor can be multiplied. These signals are then compared with their corresponding reference signals and using proper controllers, the PWM signals are generated for the front-end converter. The PWM pulses are provided to S_A and S_B as shown in Fig 4.2 for achieving regulated voltage or current at the output of the front-end converter and the PFC operation at the input grid side.

4.5.1 CC Mode

In CC mode, a constant amount of current is dumped into the battery. When the HF inverter is operated with a suitable fixed duty ratio and the input excitation is a constant DC voltage source, it delivers sinusoidal AC current with constant magnitude throughout the range of load variations, for which it is designed. The battery terminal current is sensed and compared with its reference value and corresponding PWM signals are generated to maintain constant voltage at the input of HF inverter. The corresponding control scheme is shown in Fig. 4.6.

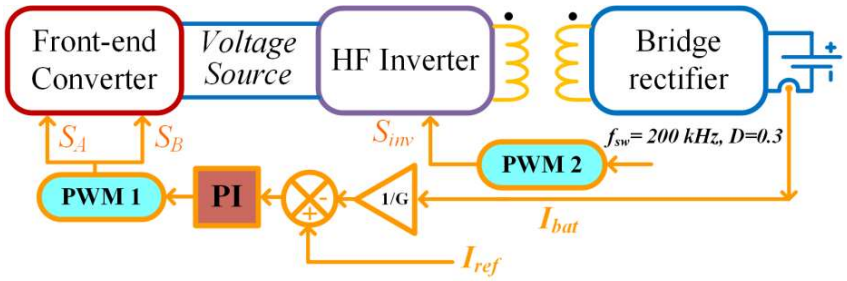

Fig. 4.6. Control scheme for CC mode of operation.

4.5.2 CV Mode

During CV mode, the battery is charged with a constant terminal voltage, where the charging current decreases gradually with the increase in state of charge (SoC) of the battery. To support this, the charger should deliver power, while maintaining the output voltage constant. For maintaining constant voltage at the battery terminal, the HF inverter should be capable to provide constant voltage at its output. As discussed earlier, the front-end converter is operated to act as a source of constant DC current for the inverter.

In this mode, the battery terminal voltage (V_{bat}) is compared with its reference value (V_{ref}) and then fed to the PI controller. Similar way to CC mode, in CV mode also the PI controller generates the required PWM signal in order to make the front-end converter as a source of constant current to feed the HF inverter as shown in Fig. 4.7.

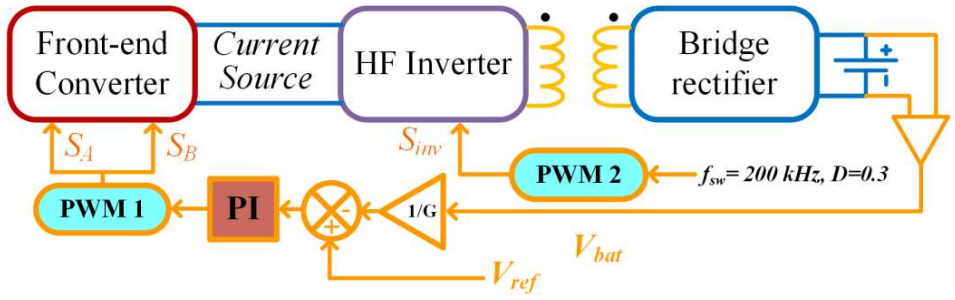

Fig. 4.7. Control scheme for CV mode of operation.

During both the modes, the HF inverter operates at a constant duty ratio. The CC-CV logic is implemented to decide the mode of operation according to the SoC of the battery. During low SoC, the battery is charged with a constant current and during high SoC, the battery is charged with a constant voltage. Accordingly, the front-end converter is operated to behave as a regulated source of current or voltage. A single PI is sufficient to deliver power to the inverter at regulated voltage or current during both CC and CV modes.

It is necessary to maintain near unity power factor at the input side as the proposed wireless charger taps power from the single-phase supply for charging the EV battery pack. To implement PFC operation at the grid side, the input AC voltage and current are sensed and fed to the PFC controller. The combined efforts of PI and PFC controller are then fed to the PWM block. The final PWM signals are fed to the gate driver circuits of two lower switches of the front-end converter. The complete control scheme for the proposed wireless charger is implemented using a TMS320F28335 DSP kit as shown in Fig. 4.8.

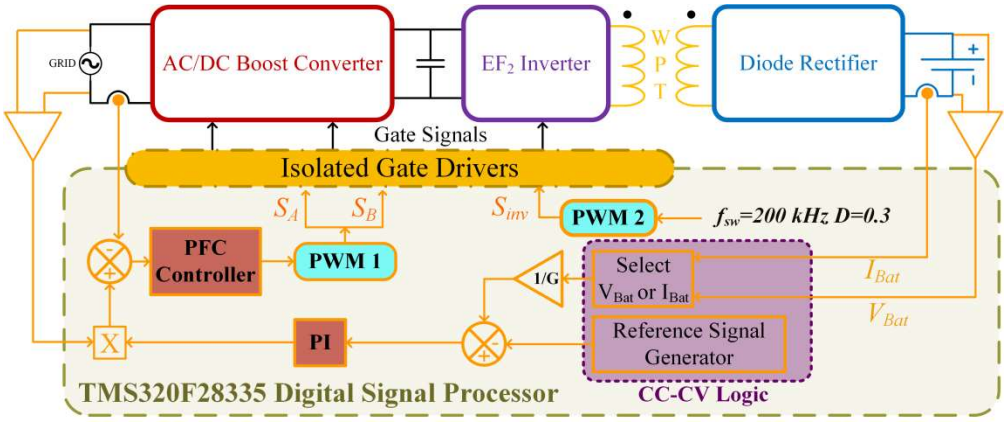

Fig. 4.8. Control schematic for the proposed wireless EV charger.

4.6 Experimental Verification

The WPT coils are first designed using ANSYS Maxwell package as shown in Fig. 4.9. Considering the leakage and mutual inductances from ANSYS, the complete topology is simulated using PSIM to verify the constant current and constant voltage properties of the proposed charger. The corresponding results for CC and CV modes are given in Fig. 4.10 and Fig. 4.11, respectively. A scaled-down laboratory prototype of the proposed wireless charger is developed to verify the charging of a 24 V, 30Ah battery set. The complete experimental set-up is shown in Fig. 4.12. The proposed wireless EV charger is also verified in the laboratory with a resistive load to transfer 200 W power for a distance of 12 cm between the transmitting and receiving coils. A 4.5mH inductor is used at the input AC side to boost the input voltage and to smoothen the ripples in the input AC current.

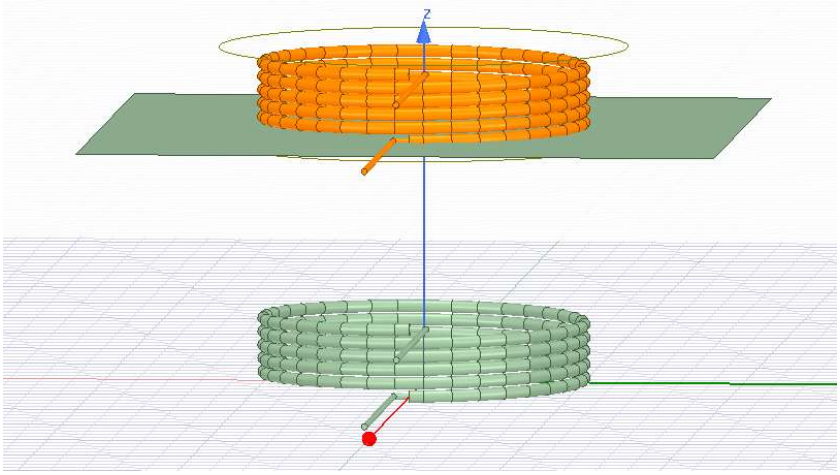

Fig. 4.9. Coil structure designed using Ansys Maxwell package.

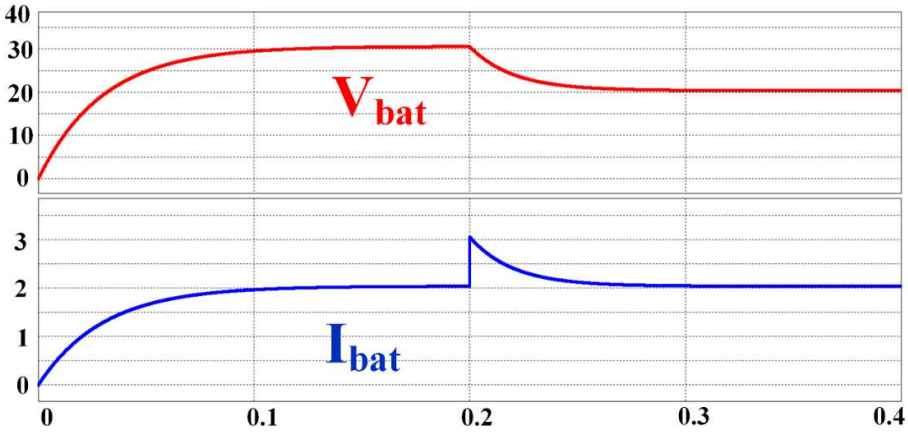

Fig. 4.10. Simulation results of the proposed charger validating CC mode.

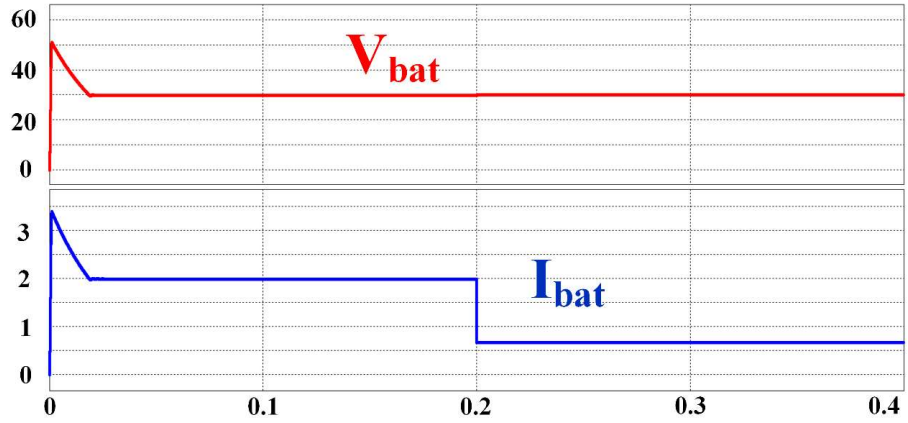

Fig. 4.11. Simulation results of the proposed charger validating CV mode.

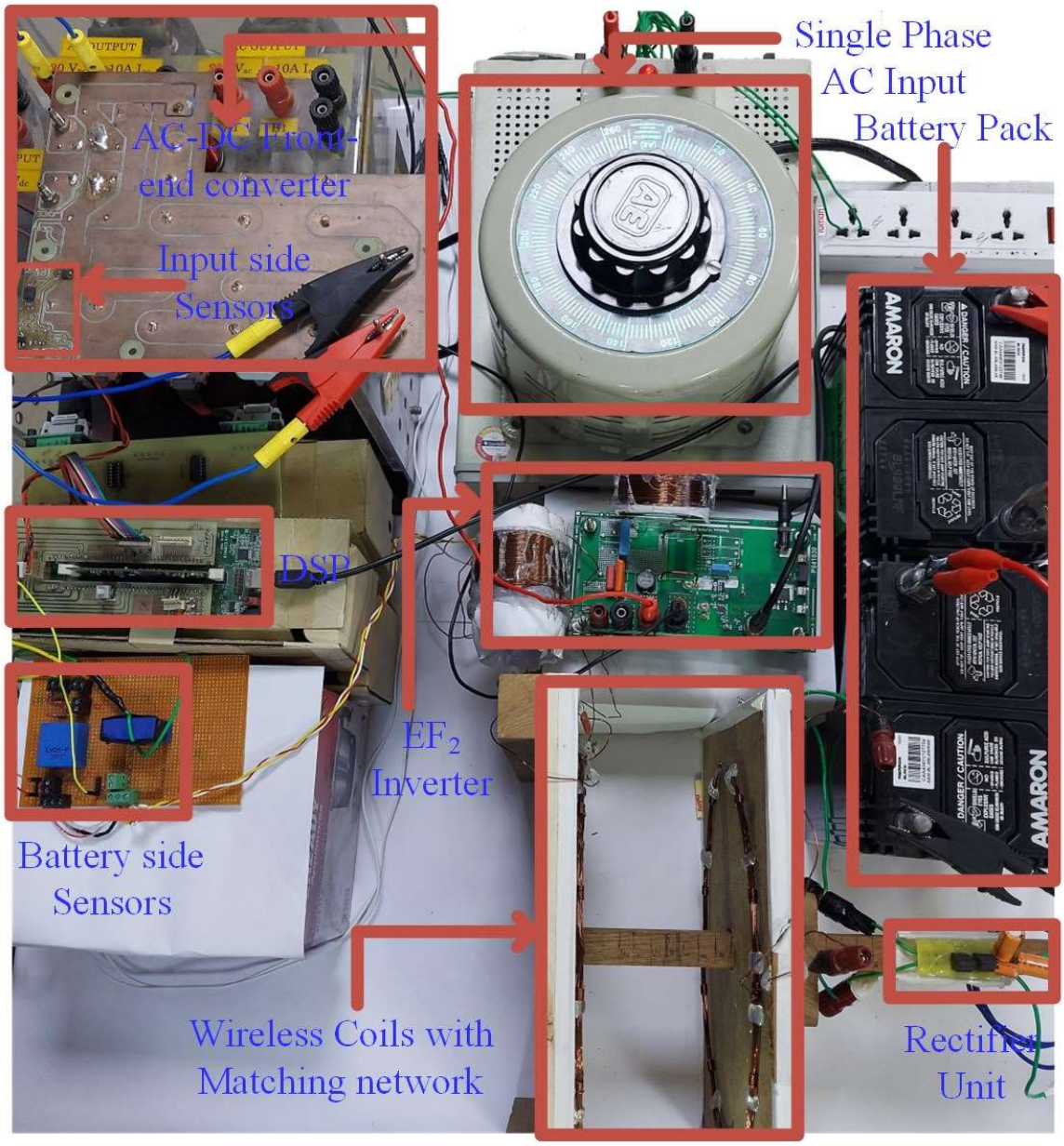

Fig. 4.12. Experimental set-up to verify the proposed idea.

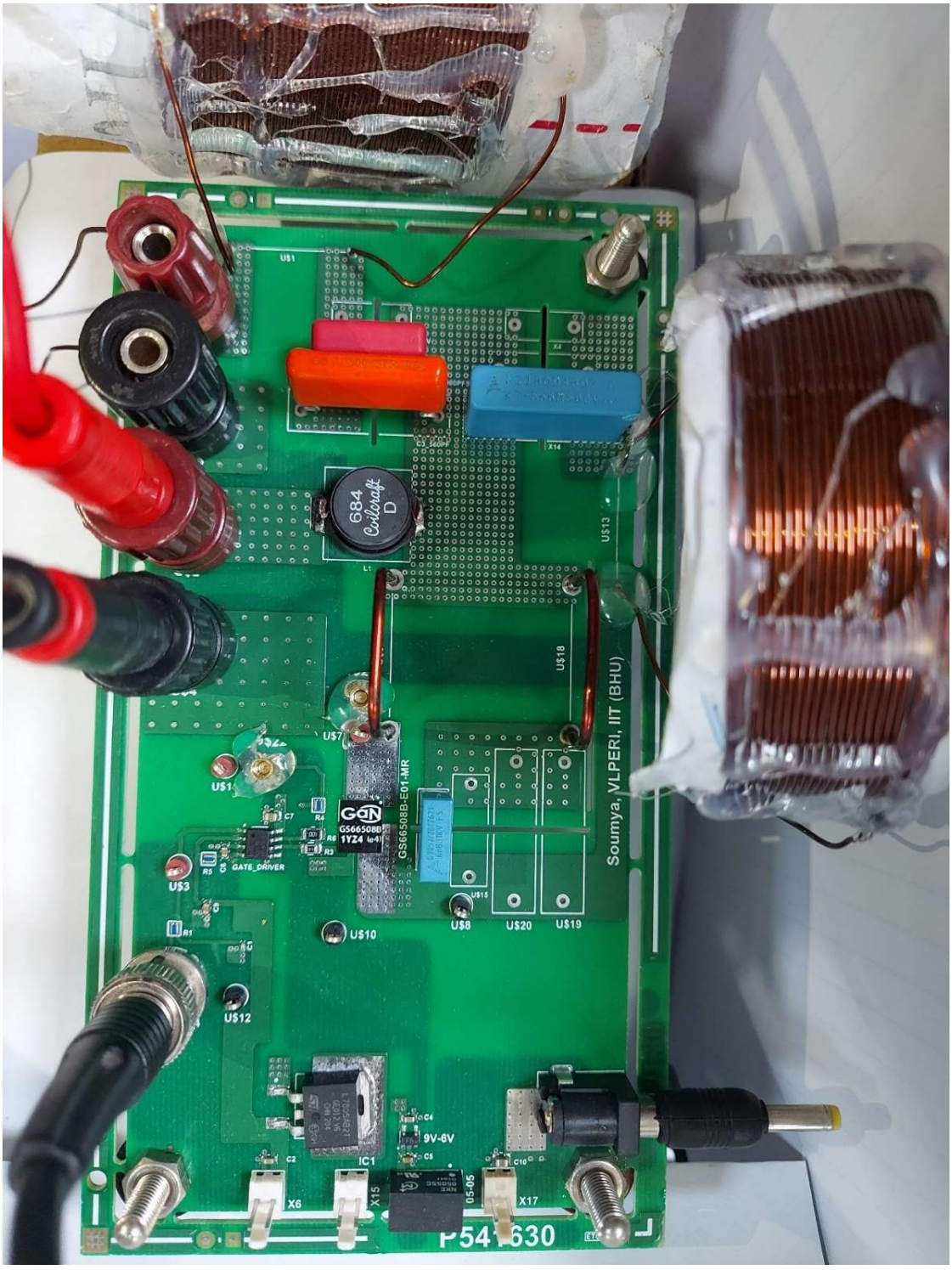

Fig. 4.13. Four layer PCB for implementing EF_2 inverter using GaN device.

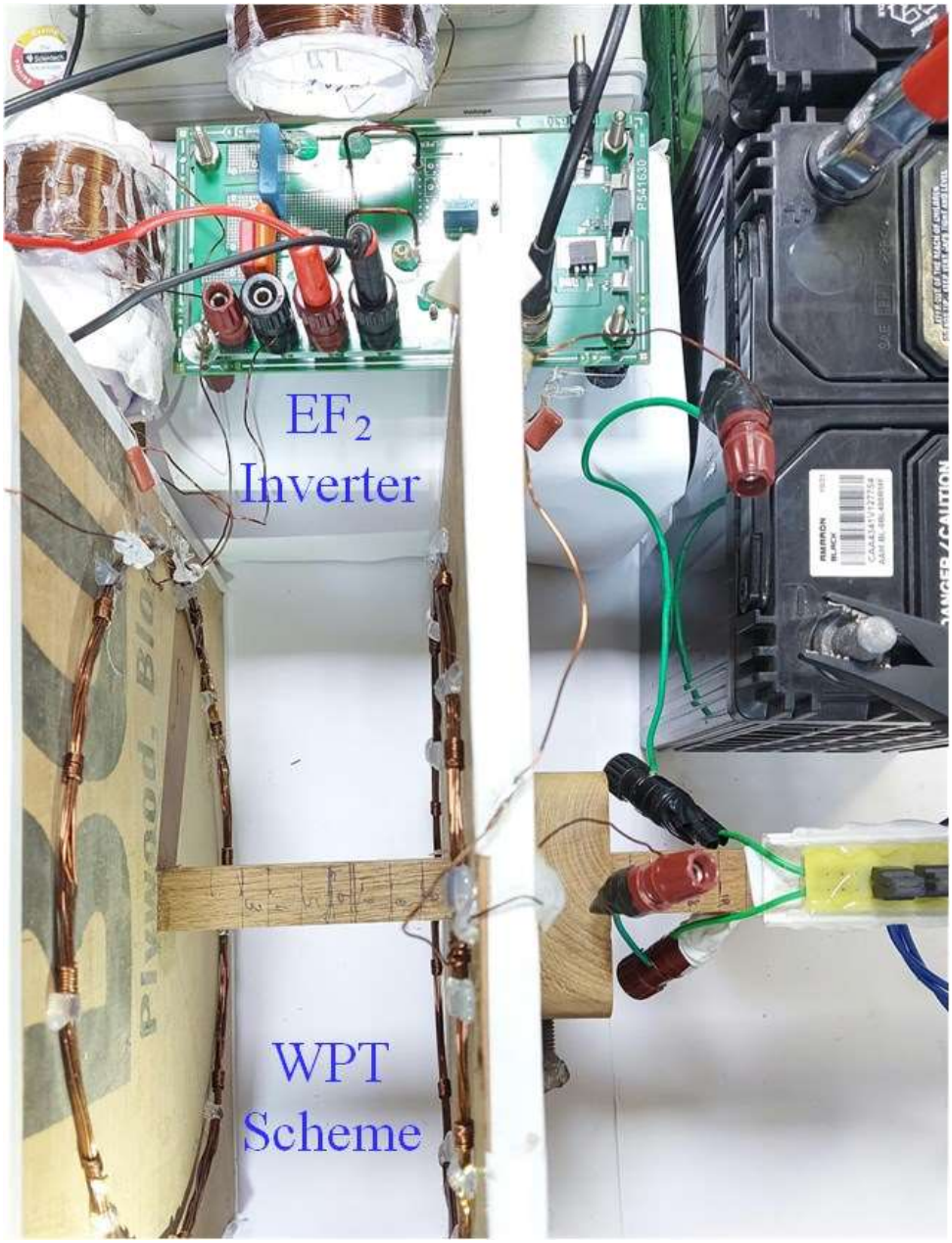

Fig. 4.14. The WPT section showing the transmitting and receiving side coil.

A Semikron IGBT module is used to realize the AC-DC boost stage. The circuit parameters of EF_2 inverter are derived for a switching frequency of 200 kHz and the corresponding values are given in Table 4.2. The WPT coils are designed according to the ANSYS design and connected at the output terminals of EF_2 inverter as shown in Fig. 4.12. The clear view of the PCB implementing EF_2 inverter using a GaN MOSFET is shown in Fig. 4.13. The WPT section with transmitting and receiving side coils is shown in Fig. 4.14.

Table 4.2. Parameters for EF_2 Inverter

Parameter	Rating
L_1	680 µH, 1200 mA
C_1	6800 pF, 1 kV
L_2	42 µH
C_2	5600 pF, 500 V
L_3	160 µH
C_3	5030 pF

A four-layered FR4 PCB board is designed to implement the EF_2 inverter as shown in Fig. 4.13. Special care is taken while fabricating the SMD component using GaN MOSFET. The GaN device is assembled on the board by properly following the reflow soldering process. An enhancement mode high electron mobility transistor (E-HEMT) GS66508B is used as S_{inv} for the HF inverter, which is a bottom-side cooled device. The recommended gate voltage range is 0 V to +6 V for the optimal performance of the GaN device used in this work. For operating the GaN MOSFET, Si-8271-GB-IS with proper biasing is used as the gate driver circuit. The bulky ferrite core-based inductors are replaced by lightweight air-core inductors to avoid saturation at high frequency operation, except for L_1 as this is only responsible to reduce the current ripple at DC side of the inverter. A 684 µH SMD inductor is used as the input inductor L_1 to reduce the ripple content of the input DC current. The air-core inductors (L_2 and L_3) are designed using enamel painted single strand copper wire of diameter 0.85 mm. Metalized polypropylene capacitors are used in the prototype to support high frequency operation. The rating of inductors and capacitors used are given in Table 4.2.

4.6.1 Operation of EF_2 Inverter

The EF_2 inverter is operated at a switching frequency of 200 kHz and the results are shown in Fig. 4.15. V_{GS} shows the gate pulse to GaN device and V_{DS} shows the drain to source voltage of the GaN device, while I_{OUT} shows the output current supplied by the inverter. The output current is sinusoidal and its frequency is same as the switching frequency. The voltage across the switch V_{DS} confirms the ZVS operation of the inverter.

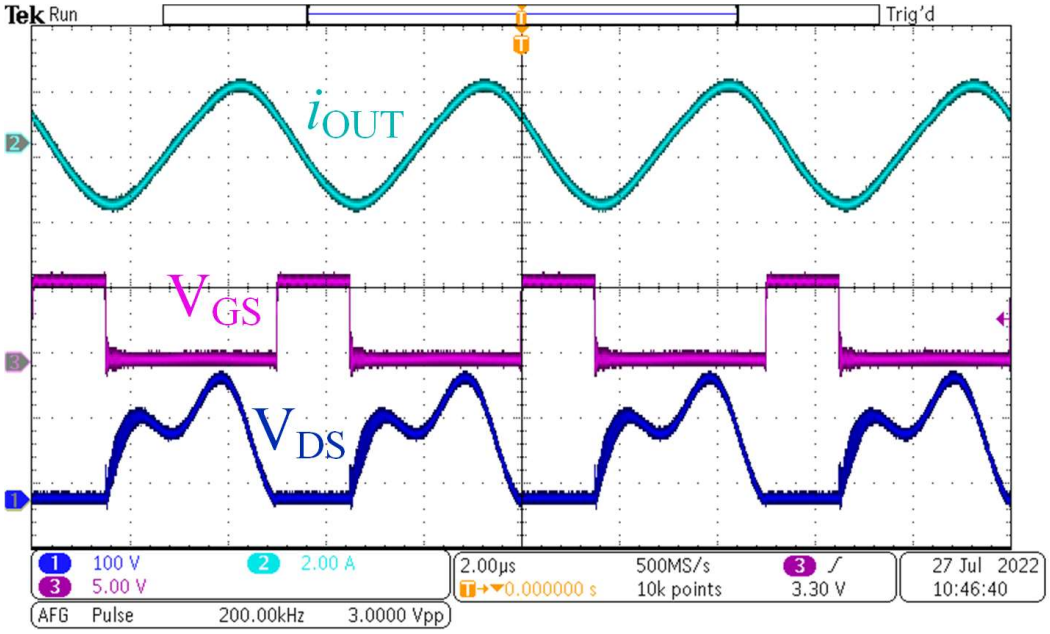

Fig. 4.15. Operation of EF_2 inverter with HFAC output current and satisfying ZVS condition.

4.6.2 Proposed Charger with Resistive load

The charger is verified with resistive load to ensure smooth operation for all probable conditions before charging the battery. Steady-state operation showing output voltage and current (V_0 and I_0) for a 20 Ω load while maintaining the ZVS condition is shown in Fig. 4.16. The transmitting side HFAC voltage and current along with voltage and current at the output terminals are shown in Fig. 4.17. Use of proper matching networks at both the transmitting and receiving sides results in perfect sinusoidal voltage and current at the transmitter side. The charger is tested at about 200 W to transfer power wirelessly to a 20 Ω load. The corresponding results are shown in Fig. 4.18, where the ZVS condition is achieved with 61 V output voltage and 3.12 A of output current.

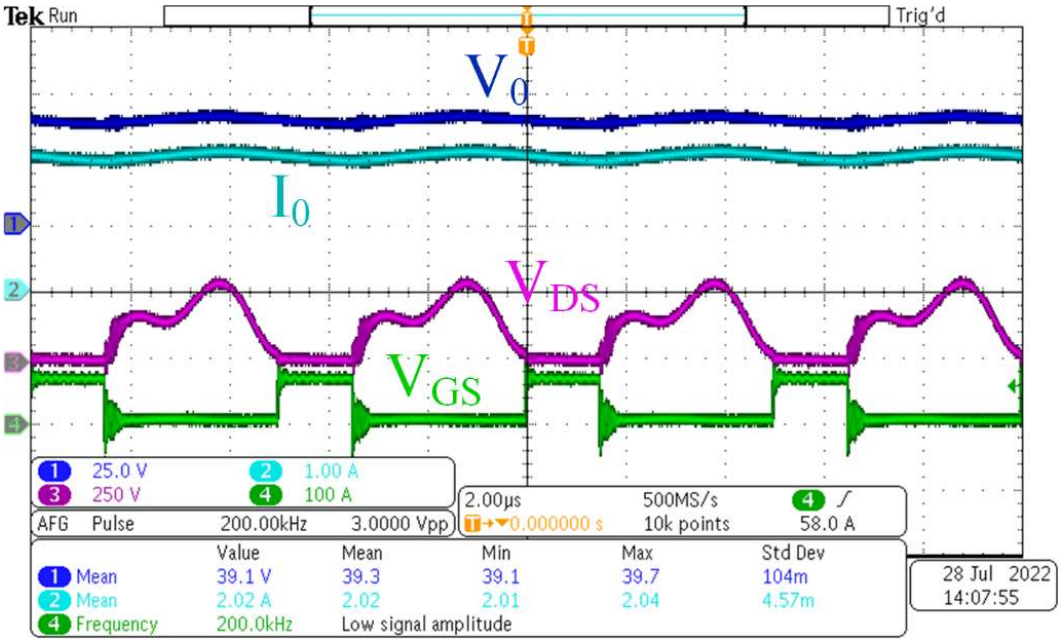

Fig. 4.16. Steady-state operation of proposed wireless charger with resistive load.

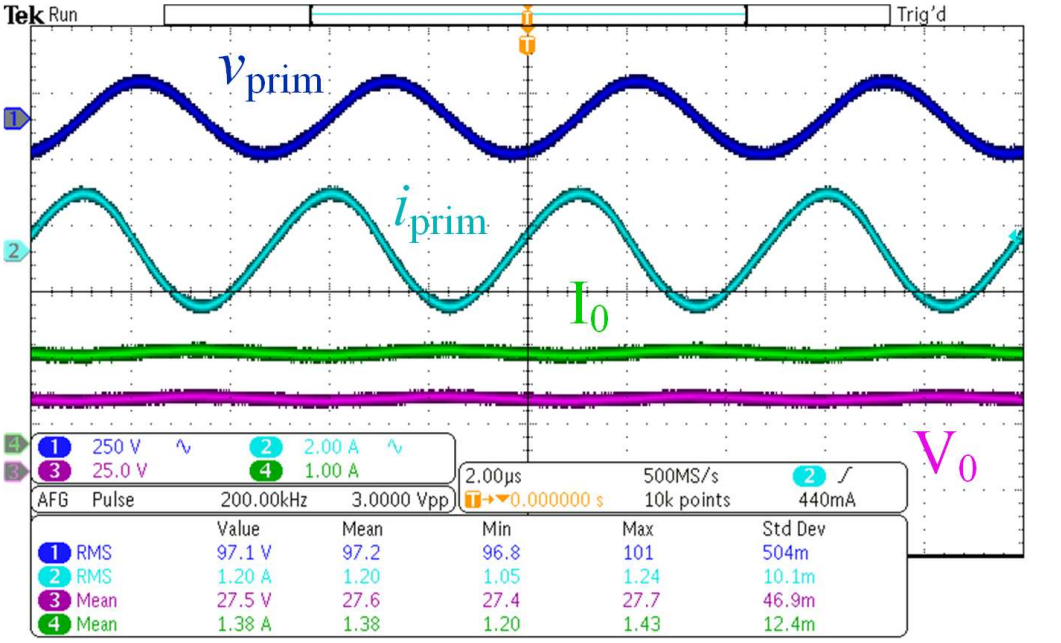

Fig. 4.17. Steady-state operation of proposed wireless charger with resistive load showing primary side voltage and current with output terminal voltage and current.

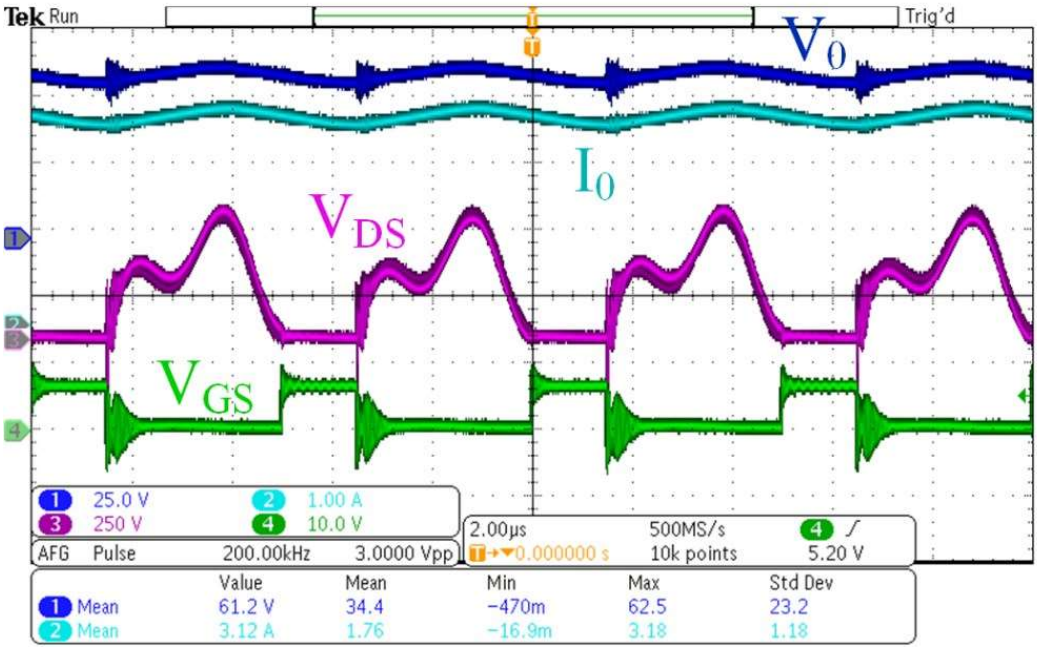

Fig. 4.18. Steady-state operation of proposed wireless charger supplying 191 W wirelessly to a resistive load.

4.6.3 Charging a 12 V Lead Acid Battery

A 12 V lead acid battery is charged to verify the validity of the proposed wireless charger. The CC-CV logic is designed to dump constant current of 1.11 A in CC mode and maintain a constant voltage of 14.5 V during CV mode. The Fig. 4.19 shows the CC mode and the Fig. 4.20 shows the CV mode, where the charging current is decreasing gradually maintaining a constant voltage of 14.5 V.

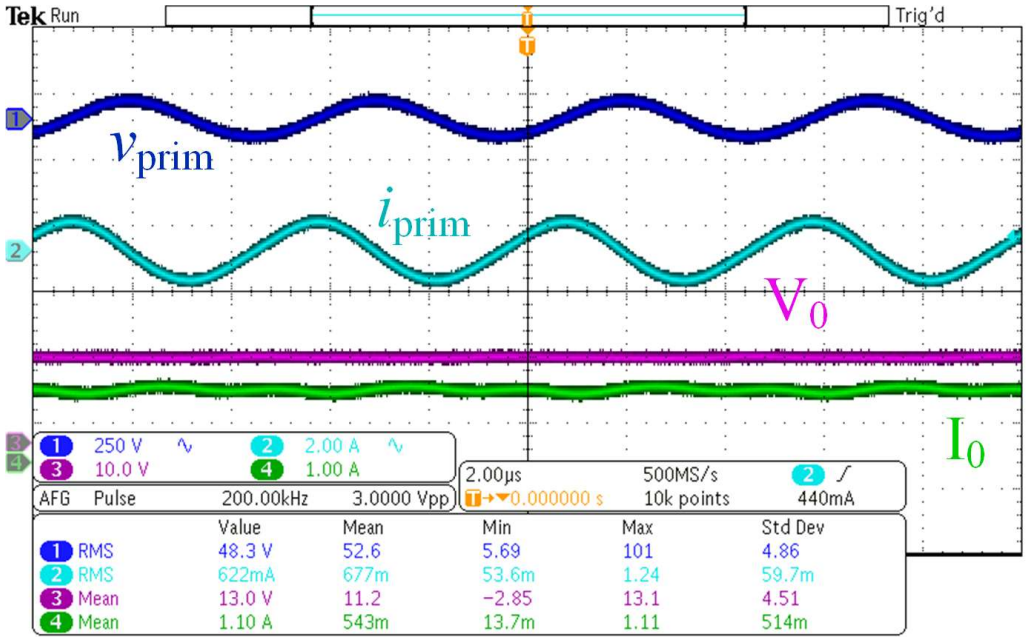

Fig. 4.19. Primary side parameters with terminal voltage and current while charging the 12 V battery in CC mode.

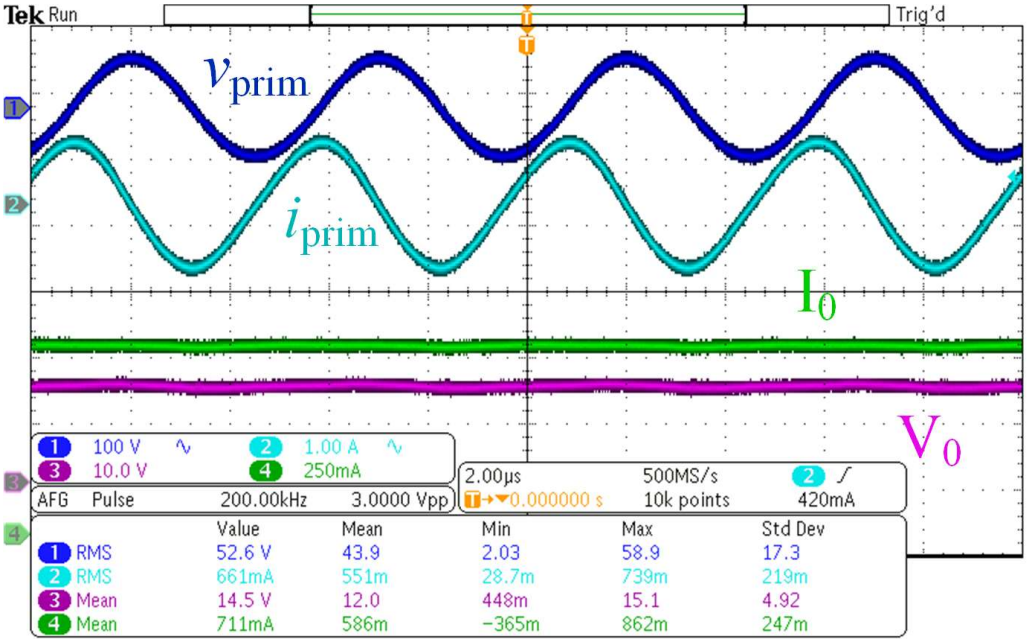

Fig. 4.20. Primary side parameters with terminal voltage and current while charging the 12 V battery in CV mode.

4.6.4 Charging a 24 V Lead Acid Battery

Finally, the proposed wireless charger is validated for a 24 V, 30 Ah battery set to obtain the CC-CV profile. The waveforms at different nodes are captured and discussed in this sub-section. The Fig. 4.21 shows that the battery is charged in CC mode with a current of 1A and the result is captured when the battery terminal voltage had reached 26.3 V. The transmitting side voltage and current during this period are also found to be sinusoidal and the frequency is same as the switching frequency. The proposed charger draws power from the grid utility, while maintaining near unity power factor at the grid side as shown in Fig. 4.22 (a). The zoomed view of Fig. 4.22 (a) is shown in Fig. 4.22 (b) to verify the sinusoidal nature of current delivered by the HF inverter as well as its smooth ZVS operation. The Fig. 4.23 (a) and (b) show the PFC operation at the input side of the proposed charger and the sinusoidal voltage and current at the transmitting side of the WPT system.

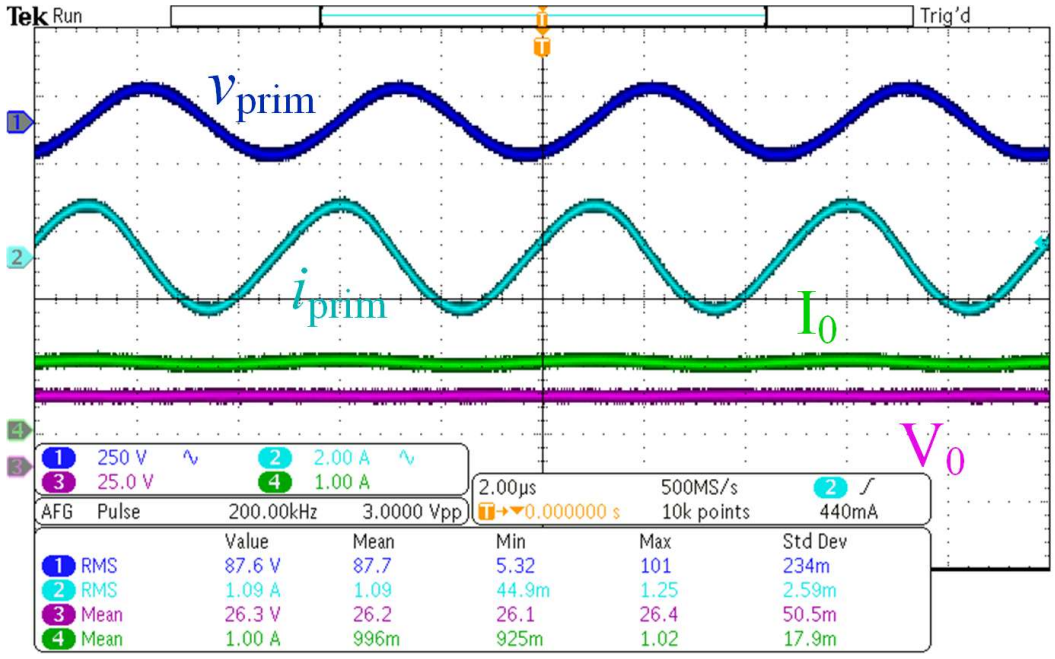

Fig. 4.21. Primary side parameters with terminal voltage and current while charging the 24 V battery.

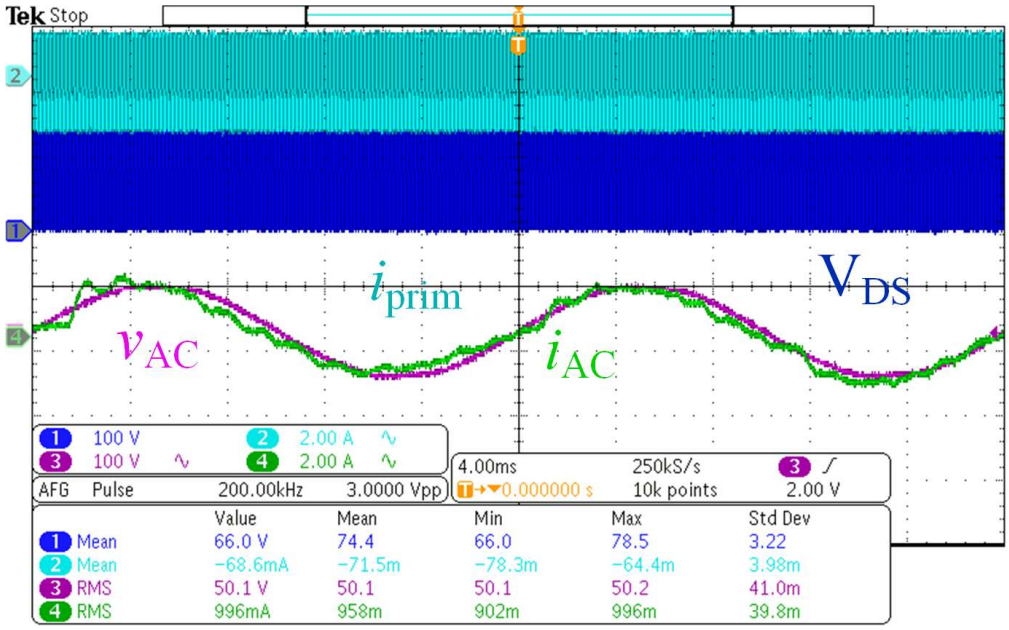

(a)

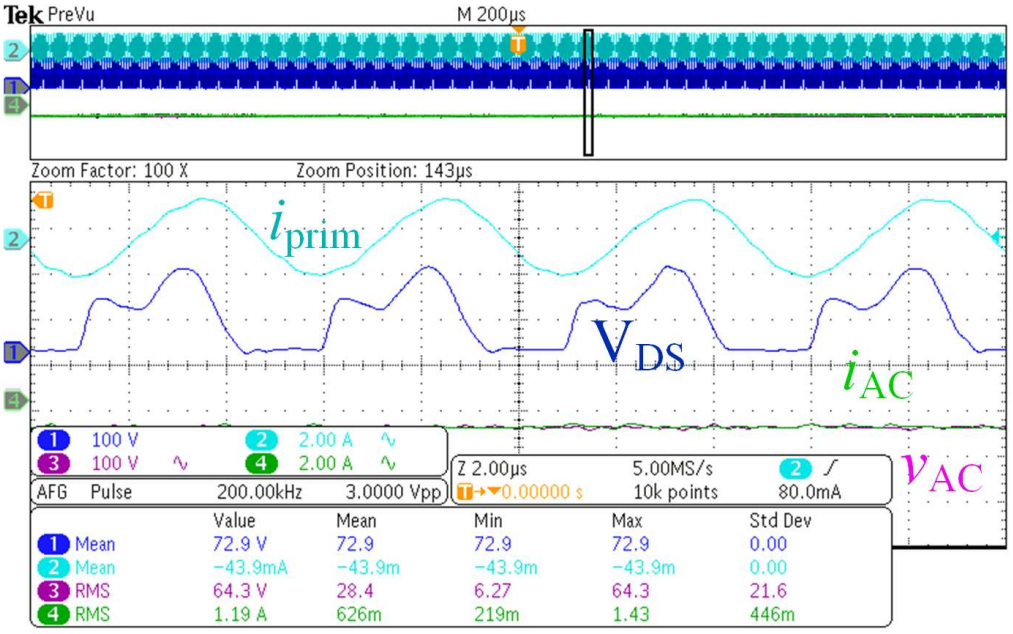

(b)

Fig. 4.22. Operation of proposed charger with 24 V battery. (a) PFC at grid side (b) ZVS of the EF_2 inverter in zoomed view.

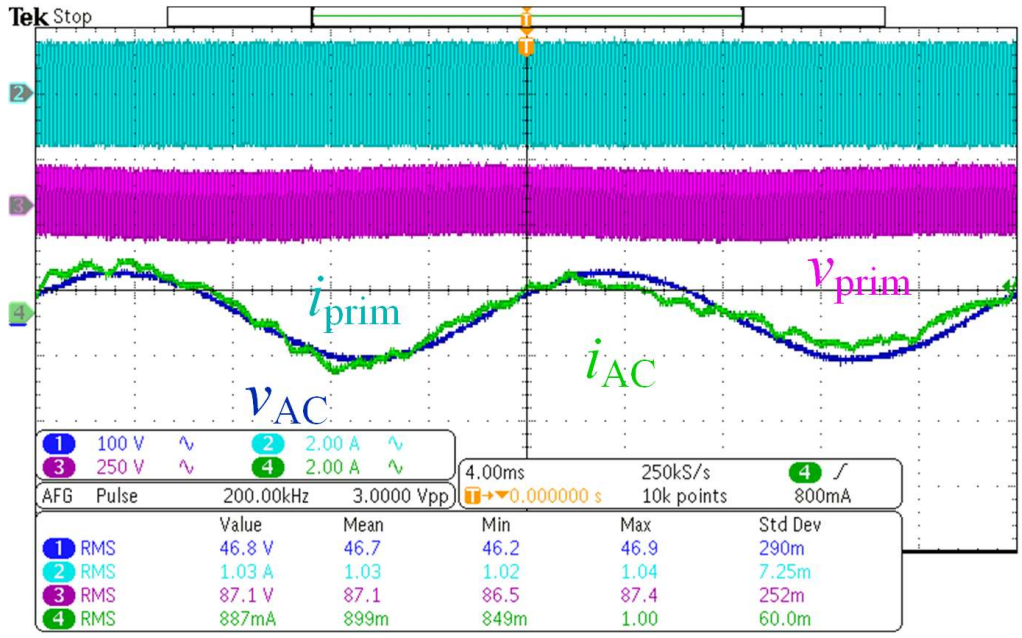

(a)

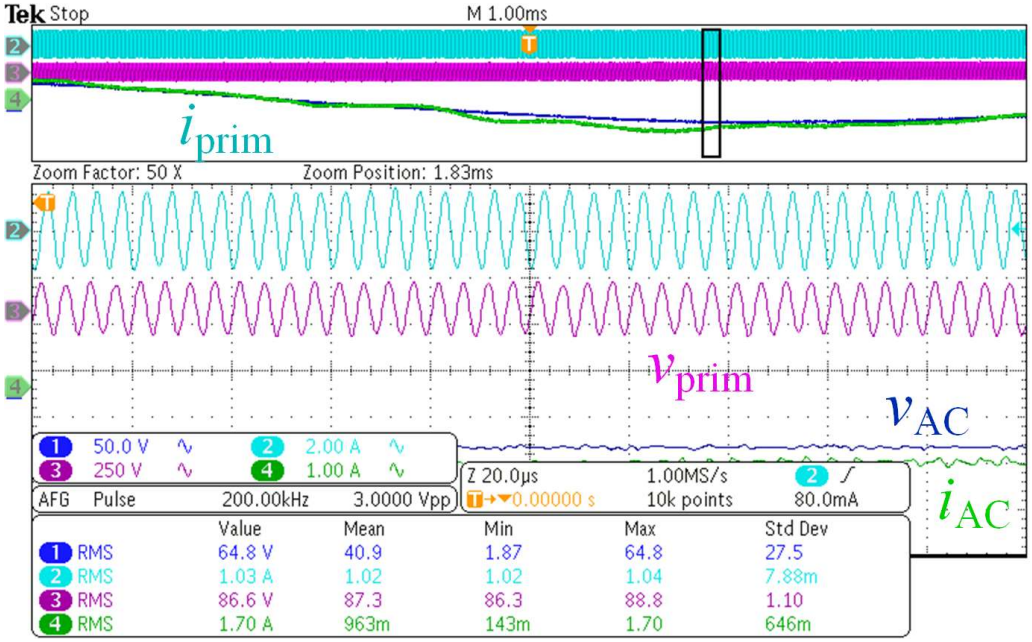

(b)

Fig. 4.23. Operation of proposed charger tapping power from the grid maintaining while PFC and showing voltage and current of transmitting side in zoomed view while charging the 24 V battery.

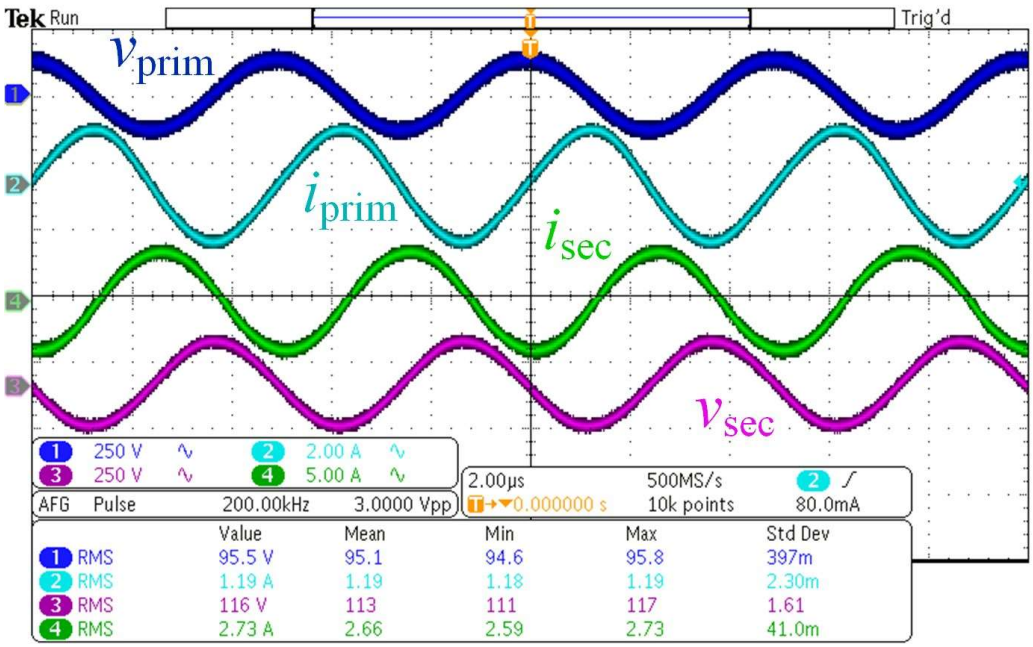

Fig. 4. 24. Operation of Wireless Power Transfer Shame showing transmitting and receiving side voltages and currents while charging the 24 V battery.

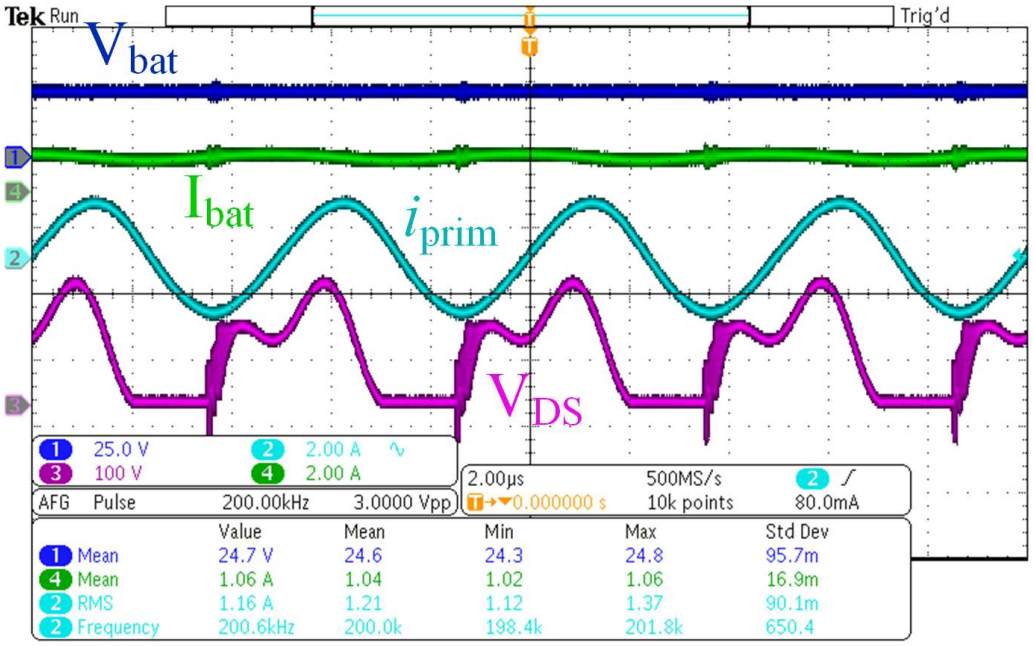

Fig. 4. 25. Battery terminal voltage and current demonstrating ZVS operation with sinusoidal output current of EF_2 inverter.

The Fig. 4. 24 shows both the transmitting and receiving side voltage and current during charging of the 24 V, 30 Ah battery set. This confirms the perfect wireless power transfer and selection of appropriate matching network parameters associated with it. The battery terminal voltage and current with primary side current of EF_2 inverter satisfying ZVS operation is shown in Fig. 4. 25.

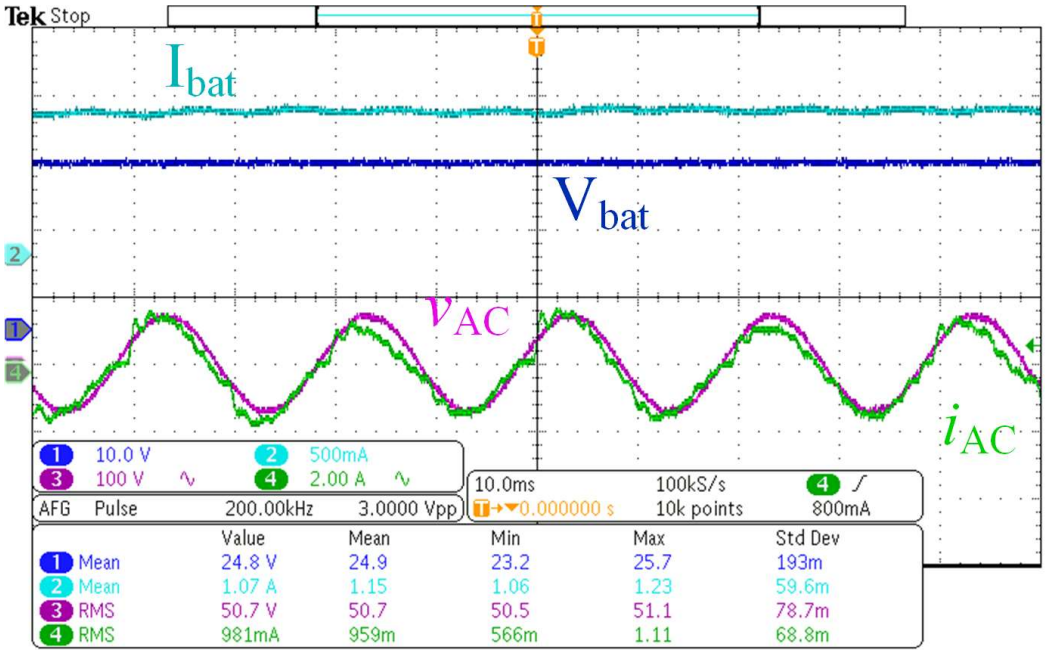

Fig. 4.26. Battery terminal parameters with input side voltage and current maintaining near UPF at the grid side.

The grid side input to the charger and its battery terminal output, while charging the 24V, 30 Ah battery is shown in Fig. 4.26. This shows that a constant amount of current is dumped into the battery during low SoC, while maintaining near unity power factor at the input side. The CC-CV profile, while charging the 24 V battery set is shown in Fig. 4.27, which confirms the implementation of CC-CV charging technique.

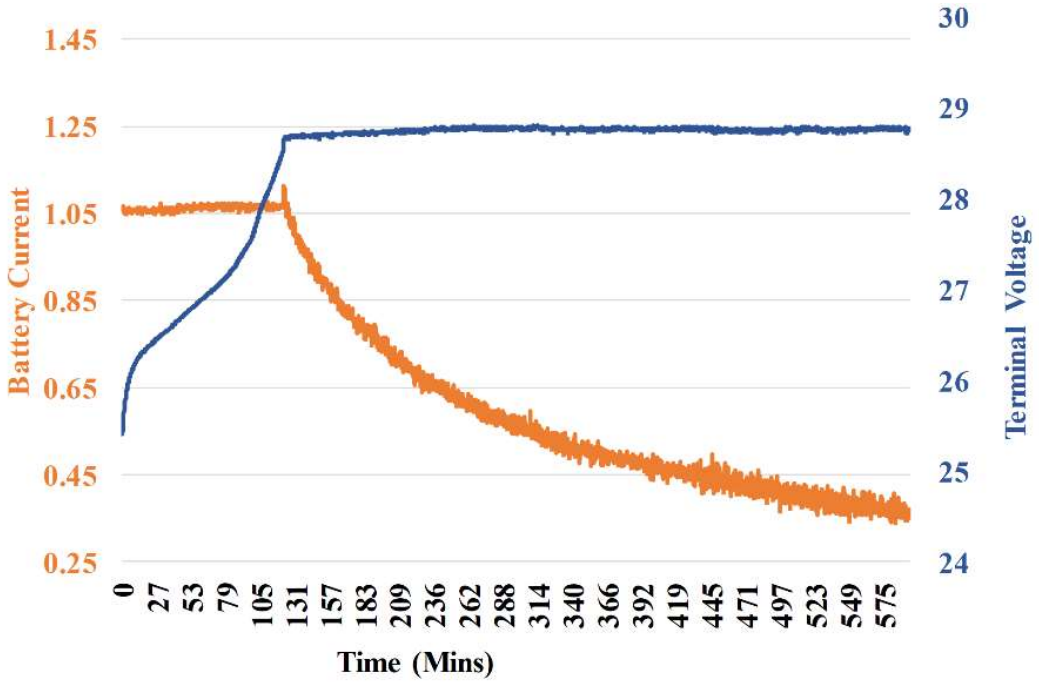

Fig. 4.27. CC-CV charging profile of the 24 V, 30 Ah battery.

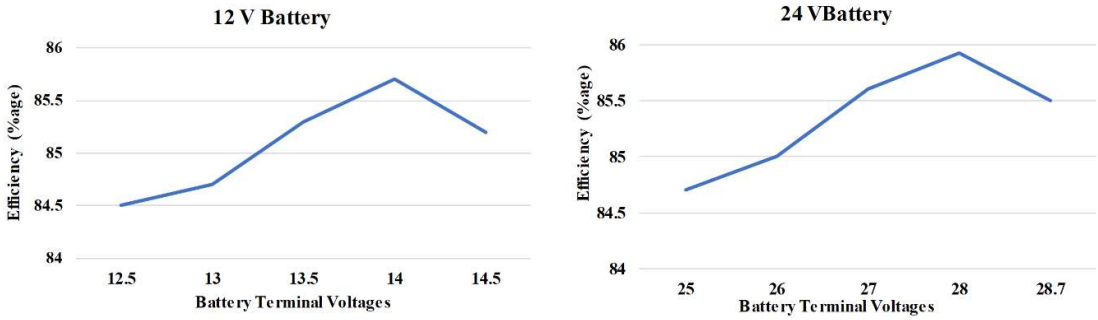

(a) (b)

Fig. 4.28. Efficiency curve during charging of a (a) 12 V and (b) 24 V battery.

The efficiency of the complete setup is measured during charging of both 12 V and 24 V batteries at different terminal voltages. The efficiency curves for both the batteries are shown in Fig. 4.28. While charging the 24 V battery, the losses in the transmitting side converter is found to be 13.6 W, while delivering 212.9 W of power. The coil-to-coil efficiency during this test set-up is found to be 92.49% and the receiving side rectifier efficiency is 96.96%.

4.7 Conclusion

A wireless battery charger for EV applications is presented in this chapter. The proposed topology is capable to charge the EV battery pack wirelessly by tapping power from a single-phase wall outlet available in domestic premises. The control scheme of the charger ensures PFC operation at the input grid side along with CC-CV charging of the battery. During the CC mode, the AC-DC stage supplies DC power at constant voltage to the EF_2 inverter, which produces constant AC current at high frequency. At the receiving side, this constant HFAC current is rectified to charge the battery with constant DC current. Similarly, during CV mode the EF_2 inverter is fed by the AC-DC stage with constant current for producing constant HFAC voltage at the output of the inverter. The constant AC voltage at high frequency is then rectified by the rectifier unit to charge the battery with constant DC voltage. The WPT coils are first simulated using Ansys Maxwell and the value of leakage inductances and mutual inductances are used to simulate the complete charger in PSIM simulation platform. A scaled-down experimental prototype is developed in the laboratory to verify the proposed charger and tested to transfer 200 W power wirelessly over a distance of 12 cm. Finally, a 12 V, 30 Ah and a 24 V, 30 Ah batteries are charged wirelessly using the proposed charger.

The proposed solution in this chapter has all the standard features of a wireless EV charging system that can be directly used as a domestic load. It may be observed that despite of all the advantages, the proposed solution requires one more power processing unit to be carried with the vehicle, which is HFAC to DC rectifier unit. To reduce the need of this additional power processor in the vehicle, the aim is to integrate this rectifier unit to the on-board power processing unit so that a single power processor can cater all three requirements during three modes of operations, which are propulsion, wired charging and wireless charging. In order to solve this issue, a new topology is presented in the next chapter.